



Full Text View

[Volume 32, Issue 5 \(May 2002\)](#)
Journal of Physical Oceanography

 Article: pp. 1536–1553 | [Abstract](#) | [PDF \(1023K\)](#)

A Mean Synoptic View of the Subantarctic Front South of Australia

Helen E. Phillips*
Institute of Antarctic and Southern Ocean Studies, University of Tasmania, Hobart, Tasmania, Australia
Stephen R. Rintoul
Antarctic Cooperative Research Centre and CSIRO Division of Marine Research, Hobart, Tasmania, Australia

(Manuscript received December 12, 2000, in final form September 18, 2001)

DOI: 10.1175/1520-0485(2002)032<1536:AMSVOT>2.0.CO;2

ABSTRACT

A mean synoptic view of the subantarctic front (SAF) is obtained from current meter and hydrographic data by averaging absolute and baroclinic velocity measurements in bins defined by a cross-stream coordinate that moves with the current. The cross-stream coordinate is derived from current meter measurements of vertical shear of the horizontal velocity and is expressed in terms of specific volume anomaly at 780 dbar (δ_{780}). By averaging absolute and baroclinic velocity measurements in stream coordinates, the spatial smoothing that results from Eulerian averaging of measurements of a meandering current is avoided. The mean SAF velocity profile is composed of one central peak and several smaller peaks. In the central peak, the 2-yr mean absolute velocity from current meters reaches 52 cm s^{-1} at 420 dbar; the mean baroclinic velocity from six CTD sections reaches 34 cm s^{-1} . The SAF flow is coherent at all levels, reaches the seafloor, and is at least 220 km wide. The cross-stream structure of baroclinic and absolute transport of the SAF has been characterized for the first time. The integrated mean transport is $116 \pm 10 (\times 10^6 \text{ m}^3 \text{ s}^{-1})$, of which approximately 14% is barotropic, where barotropic transport is defined to be the velocity at the deepest current meter (3320 dbar) multiplied by the water depth. Comparison of the current meter measurements with hydrographic sections suggest this estimate is likely a lower bound on the absolute transport, as part of the “cold side” of the SAF is not sampled by the moored array. Linear conditions for baroclinic and barotropic instability of the mean flow are satisfied at the array, consistent with earlier work that showed baroclinic conversion is the dominant mechanism for eddy growth at the array, with weaker barotropic conversion also occurring.

Table of Contents:

- [Introduction](#)
- [Data](#)
- [Mean absolute velocity](#)
- [Mean baroclinic velocity](#)
- [Transport structure](#)
- [Linear instability analysis](#)
- [Discussion](#)
- [Summary and conclusions](#)
- [REFERENCES](#)
- [APPENDIX](#)
- [TABLES](#)
- [FIGURES](#)

Options:

- [Create Reference](#)
- [Email this Article](#)
- [Add to MyArchive](#)
- [Search AMS Glossary](#)

Search CrossRef for:

- [Articles Citing This Article](#)

Search Google Scholar for:

- [Helen E. Phillips](#)
- [Stephen R. Rintoul](#)

The Antarctic Circumpolar Current (ACC) is a strong, deep-reaching current that provides the main connection between the Pacific, Atlantic, and Indian Oceans. Despite its recognized importance in the global-scale ocean circulation and climate system, measurements of the transport of heat, nutrients, and other properties by the ACC are scarce due to the hostile environment and vast size of the Southern Ocean. Drake Passage is the narrowest and most studied choke point of the ACC and here alone we have an understanding of the variation in velocity across the ACC and a reliable estimate for its mean absolute transport, 134 ± 13 Sv ($\text{Sv} \equiv 1 \times 10^6 \text{ m}^3 \text{ s}^{-1}$) [[Nowlin and Klinck \(1986\)](#), based on [Whitworth \(1983\)](#) and [Whitworth and Peterson \(1985\)](#)].

At the two remaining choke points, south of Australia and south of Africa, information is limited to the baroclinic part of the velocity field, which can be estimated from hydrographic transects. By baroclinic we mean the part of the velocity field that can be determined from the density field using the geostrophic approximation and referencing to a deep level. South of Africa, several estimates have been made of the baroclinic transport, ranging from 155 Sv ([Read and Pollard 1993](#)) down to 140 Sv ([Georgi and Toole 1982](#)) and 129 Sv ([Jacobs and Georgi 1977](#)). South of New Zealand the baroclinic transport is estimated to be 125 Sv ([Georgi and Toole 1982](#)). South of Australia, six repeat hydrographic transects along WOCE section SR3 were combined to estimate a mean net baroclinic transport between Australia and Antarctica of 147 ± 10 Sv relative to a near-bottom reference level ([Rintoul and Sokolov 2001](#)).

At most locations in the Southern Ocean there are insufficient sections to estimate even the mean baroclinic velocity field. In addition, studies suggest that there is also significant barotropic flow ([Whitworth 1983](#); [Donohue et al. 2001](#)). To directly measure the absolute velocity with moored instruments across the full width of the ACC is an inordinately expensive and difficult task, particularly outside Drake Passage. Acoustic Doppler current profilers (ADCPs) do not yet measure absolute velocity with sufficient accuracy to provide a reference for transport across long sections ([Donohue et al. 2001](#)). As a result, our knowledge of the absolute velocity of the ACC remains incomplete.

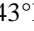
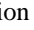
A method of profiling the Gulf Stream velocity field using a single current meter mooring was described by [Hall and Bryden \(1985\)](#). It has since been used successfully to provide a mean synoptic view of the Gulf Stream at different locations ([Hall 1986](#); [Johns et al. 1995](#); [Bower and Hogg 1996](#)) and of the Kuroshio ([Hall 1989](#)). The method relies on the assumption that the cross-stream structure of the current is fixed in time although the current stream is free to move in any direction. As the current meanders back and forth over the fixed mooring, the current meters measure velocity at different locations in the cross-stream direction. The individual measurements are then combined to construct a mean cross-stream profile of the current, which is synoptic in the sense that the full strength and the width of the current are accurately represented. Averaging in a fixed geographic coordinate frame, assuming enough of the current has been instrumented to allow this kind of averaging, results in a broader, weaker profile ([Bower and Hogg 1996](#)) since the geographic location of the maximum in the geographic mean profile is at times occupied by the strongest part of the current and at other times by the weaker edges. An alternative method for determining the cross-stream location of the current axis was described by [Hogg \(1992\)](#).

In this paper we explore for the first time the applicability of streamwise profiling techniques to the ACC. We use a modified version of the [Hall and Bryden \(1985\)](#) method to derive a mean cross-stream profile of absolute velocity in the Subantarctic Front (SAF) of the ACC from current meter data. [Rintoul and Sokolov \(2001\)](#) show that the SAF is the main core of the ACC south of Australia in terms of baroclinic flow. We also introduce a second profiling method that uses a predetermined cross-stream coordinate to produce a mean cross-stream profile of baroclinic velocity in the SAF from hydrographic data.

Following the introductory sections, the two profiling techniques and the resultant mean profiles are described in [sections 3 and 4](#). Absolute and baroclinic volume transport per unit width across the SAF are examined, and the barotropic transport is estimated in [section 5](#). We also briefly examine the linear conditions for barotropic and baroclinic instability in the SAF in [section 6](#). The results of the earlier sections are brought together in [section 7](#) and are compared with estimates of velocity and transport at other locations in the ACC. The paper concludes with a summary ([section 8](#)).

2. Data

a. Current meter

The AUSSAF array consisted of four tall current meter moorings deployed during March 1993 and recovered in January 1995, near $50^{\circ}30' \text{ S}$, 143°E ([Fig. 1](#) ). The moorings form the shape of a “T,” oriented such that three moorings, called North, Central, and South, lie 35 km apart along WOCE section SR3, perpendicular to the climatological SAF and centered on its mean position from [Olbers et al. \(1992\)](#). The fourth mooring, West, was placed 50 km upstream of the main line to allow for the determination of alongstream gradients. In [Fig. 1](#) , the background shading shows the bathymetry ([Smith and Sandwell 1994](#)), and the white lines are surface dynamic heights relative to 2000 dbar, calculated from the [Olbers et al. \(1992\)](#) atlas. The array sits in approximately 3800 m of water on the northern flank of the Southeast Indian Ridge, downstream of the point where the ridge turns southeastward. The [Olbers et al. \(1992\)](#) climatology shows that the ACC also turns southeastward, upstream of the array.

In total, 18 Aanderaa current meters were deployed at nominal depths of 300, 600, 1000, 2000, and 3200 m on West, South, and Central, and at 1000, 2000, and 3200 m on North. All instruments measured temperature and current speed and direction; some recorded pressure. Temperature and velocity were low-pass filtered to remove all signals with periods shorter than 40 h and were then subsampled daily. Temperature and velocity at nominal depths of 1000 m and above were corrected for mooring motion, using the method of [Hogg \(1991\)](#), to constant pressure levels of 420, 780, and 1150 dbar,

the mean pressures of these instruments averaged over the array. Data from the deep instruments were left uncorrected; their mean pressures are 2240 and 3320 dbar. Dates of operation of each instrument after gaps have been filled by the mooring motion correction algorithm are shown in [Table 1](#). See [Phillips and Rintoul \(2000\)](#), hereafter referred to as PR for more details. Note that PR used the mooring motion correction scheme to simulate the entire record at West 2000 m. The simulation has been omitted from the present study since its inclusion resulted in little change to the mean velocity profiles.

b. Hydrography

Between 1991 and 1996, WOCE hydrographic section SR3 between Tasmania and Antarctica ([Fig. 1](#)) was occupied six times, sampling all seasons. Here we examine only geostrophic velocity across the SR3 section; further analyses can be found in [Rintoul et al. \(2002\)](#), [Rintoul and Bullister \(1999\)](#), and [Rintoul and Sokolov \(2001\)](#). [Table 1](#) lists the dates of occupation of SR3.

ADCP data was available on the three voyages from 1995 onward. In [section 4d](#), we compare geostrophic velocity from CTD data with ADCP data in bin 11 (100.6 m). We use the on-station ADCP data and average over the duration of the CTD downcast to obtain one ADCP velocity for each CTD station, and then average adjacent stations to compare with the geostrophic velocity between stations.

3. Mean absolute velocity from current meter data

a. Defining the cross-stream coordinate

Phillips and Rintoul examined the variability at the AUSSAF array and found that a daily varying coordinate frame that is attached to the core of the moving SAF and whose x coordinate is always in the direction of the current stream allowed a more revealing description of the velocity field and cross-stream eddy fluxes than was possible using a geographic coordinate frame. They defined the along-stream coordinate to be the direction of the vertical shear of horizontal velocity between 420 and 2240 dbar, and the cross-stream coordinate to be 90° to the left of alongstream. This definition of alongstream corresponds to the direction of the thermal wind, lying parallel to contours of dynamic height, and reliably approximates the direction of the baroclinic flow above 2240 dbar. The levels 420 and 2240 dbar were chosen because they span the depths where current shear and temperature changes are greatest. We use the same coordinate frame in this study and now take the next step of quantifying the time-varying cross-stream position of the axis of the SAF relative to the current meter array so that the cross-stream structure of the SAF can be examined.

In profiling the Gulf Stream, [Hall and Bryden \(1985\)](#) used temperature at 575 dbar (T_{575}) to determine the distance y of the stream core from their array. The thermal wind assumption and vertical shear measured by the current meters were used to infer the cross-stream gradient of temperature at 575 dbar, $\partial T/\partial y|_{575}$. Linear relationships between $\partial T/\partial y|_{575}$ and T_{575} either side of the core were integrated and inverted to yield cross-stream distance as a function of T_{575} . Velocity data were then grouped in bins of T_{575} , giving a cross-stream profile of velocity at each of the current meter levels.

We present here a modification of the [Hall and Bryden \(1985\)](#) method (N. Bindoff 1999, personal communication). The motivation for seeking an alternative was the desire to quantify the error associated with estimating the cross-stream position from the density field. In Hall and Bryden's method it is straightforward to estimate the variance in $\partial T/\partial y|_{575}$ about the linear fit. But it is unlikely that carrying this variance through the integration and inversion steps would give a reliable estimate of the variance in y . For comparison with the new method described in this paper, the mean velocity profile of the SAF using the Hall and Bryden method is presented in the [appendix](#).

We use specific volume anomaly (δ) at 780 dbar, δ_{780} , as our cross-stream coordinate since T - S relationships are not tight in the region of the SAF and we cannot assume a linear relationship between temperature and density, as is often done for the Gulf Stream. Empirical T - δ relationships for a series of pressure levels have been determined from the SR3 hydrographic data, allowing δ to be inferred from temperature measured by the current meters ([Phillips 2000](#)).

[Figure 2](#) shows alongstream velocity and temperature at 780 dbar, T_{780} , for the West, South, and Central moorings. Strong flows ($>50 \text{ cm s}^{-1}$) occur for T_{780} between 5° and 7°C . A scatterplot (not shown) of current speed versus T_{780} from all moorings combined shows that the strongest flows correspond roughly to $T_{780} = 6^\circ\text{C}$. We define the core of the SAF to be where the 6°C isotherm crosses 780 dbar, which corresponds to $\delta_{780} = 1.102 \times 10^{-6} \text{ m}^3 \text{ kg}^{-1}$. This choice of reference point is not critical to the following analyses, a point at either edge of the SAF would serve equally well but would be harder to define.


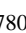
Using the thermal wind equation,

$$f \frac{\partial u}{\partial z} = \frac{-g}{(\delta + 1/\rho_p)} \frac{\partial \delta}{\partial y} \quad (1)$$

the cross-stream gradient of δ , $\partial\delta/\partial y$, is determined from the vertical shear of alongstream velocity, $\partial u/\partial z$. Here

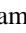
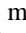

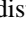
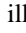
$$\delta = \frac{1}{\rho(S, T, P)} - \frac{1}{\rho_p}$$

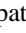
has units of $\text{m}^3 \text{kg}^{-1}$, ρ is density and $\rho_p = \rho(35, 0, P)$, z and y are the vertical (positive upward) and cross-stream (positive to the left of alongstream) coordinates, f is the Coriolis parameter ($= -1.13 \times 10^{-4} \text{ s}^{-1}$), and g is the earth's gravitational acceleration ($= 9.8 \text{ m s}^{-2}$). The balance in (1) is evaluated at 780 dbar, estimating $\partial u/\partial z$ as a finite difference between 420 and 1150 dbar.

In Fig. 3 , the reciprocal of $\partial\delta/\partial y$ at 780 dbar is plotted versus δ_{780} . We have not included the reciprocal of any points with $\partial\delta/\partial y < 0.33 \times 10^{-9} \text{ m}^3 \text{kg}^{-1} \text{ km}^{-1}$, thus the maximum $(\partial\delta/\partial y)^{-1}$ is $3 \times 10^9 \text{ km kg m}^{-3}$. This excludes approximately 2% of points, evenly distributed in δ_{780} . The predominance of low values near $\delta_{780} = 1.1 \times 10^{-6} \text{ m}^3 \text{kg}^{-1}$ marks the strongest horizontal density gradients and correspondingly the strongest flow. Although δ_{780} is our cross-stream position indicator, T_{780} is a more readily interpreted variable and, where appropriate, a T_{780} axis is also provided, as in Fig. 3 .


Sokolov and Rintoul (2001, hereafter SR) have shown, using a combination of CTD, XBT, and satellite altimeter data near 140°E, that there are multiple branches to the SAF. West of the SR3 line there are three branches, two of which (middle and southern) have merged by the longitude of SR3. Both branches at SR3 are characterized by a relatively narrow meander envelope. The Polar Front (PF) is also composed of two branches at SR3; the northern branch at times is merged with the southern branch of the SAF. We demonstrate in section 4c that the current meters do not sample the PF. Thus, the appearance of low values of $(\partial\delta/\partial y)^{-1}$ down to $\delta_{780} = 0.85 \times 10^{-6} \text{ m}^3 \text{kg}^{-1}$ is likely due to the sampling of more than one branch of the SAF.

It is clear that by integrating $(\partial\delta/\partial y)^{-1}$ with respect to δ_{780} we obtain y . However, the interesting part is choosing which path through the scatter of inverse slopes gives the best estimate of cross-stream distance and which two paths, above and below the path chosen to give y , will best represent the error in y .

A histogram of all inverse slopes (Fig. 4 ) shows that the overall distribution of points is not Gaussian; this is equally true for the distribution of points in any one δ_{780} bin. The median value, or 50th percentile, of inverse slopes in δ_{780} bins of $0.02 \times 10^{-6} \text{ m}^3 \text{kg}^{-1}$ (solid line, Fig. 3 ) is therefore chosen to give cross-stream distance. The shaded region about the median in Fig. 3  is analogous to a one standard deviation envelope for a Gaussian distribution, determined as follows. For a Gaussian distribution (inset, Fig. 4 ) the envelope of one standard deviation about the mean encloses an area under the distribution curve equal to 68% of the total area under the curve. For our non-Gaussian distribution, an area equal to 68% of the total, centered on the median, with equal area either side of the median has limits that are the 16th and 84th percentiles. Figure 4  illustrates where these percentiles fall within the overall distribution of inverse slopes, which is representative of the distribution in the smaller bins.

Having identified three paths through the scatter of inverse slopes, trapezoidal integration is used to calculate the area under each path between the origin and each δ_{780} bin to obtain y and its upper and lower errors (Fig. 5 ). The origin of integration marks the core of the stream at $\delta_{780} = 1.102 \times 10^{-6} \text{ m}^3 \text{kg}^{-1}$ (equivalent to $T_{780} = 6^\circ\text{C}$). The error in y is zero at the origin, by definition, and becomes larger toward the outer limits of the stream. We are therefore cautious in the following analysis when interpreting the behavior of the stream at its edges. Within $\pm 100 \text{ km}$ of the origin the error in y is less than 10 km.



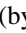
b. Mean absolute velocity profile

The mean cross-stream profile of absolute alongstream velocity at each current meter level is estimated by grouping alongstream velocity into bins of δ_{780} and averaging the velocities in each bin. The mean velocity profile (Fig. 6 ) has one main peak near $T_{780} = 6^\circ\text{C}$, reaching 52 cm s^{-1} at 420 dbar. Two shoulders to the main peak near 4°C and 7.7°C have maximum velocities of 28 and 31 cm s^{-1} at 420 dbar, respectively, and a secondary peak near 3.2°C has a maximum velocity of 26 cm s^{-1} . Near-bottom velocities (3320 dbar) are up to 3.6 cm s^{-1} in the main jet with a maximum of 5.9 cm s^{-1} on the cold side near -100 km .

The vertical coherence of the velocity at the top four current meters within the main peak is striking, although expected from the results of [PR](#). The only apparent shift in the position of the velocity maximum with depth is a slight northward shift (1 bin \approx 10 km) with increasing depth of the two cold peaks near 3.7°C (from 1150 to 2240 dbar), and near 3.2°C (from 780 to 2240 dbar). The profile at 3320 dbar is quite different to the shallow profiles and suggests an intensification of the bottom flow on the cold side, 100 km and more from the core. Phillips and Rintoul showed that the deep instrument was dominated by processes with timescales much shorter than at shallower levels, which are presumably the result of interactions with the seafloor.

The warm edge of the SAF above 1000 m is sharper than the cold edge and also has less vertical shear. There is no indication of any upstream flow in the mean profile at the four upper levels, but at 3320 dbar there is statistically significant upstream flow at the warm edge.

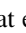
The width of the mean SAF, which we take to be the distance from the base of the main peak on the warm side near 7.5°C to the base of the shoulder on the cold side near 3.5°C, is approximately 170 km. Results from [section 5](#) will show that the mean profile misses part of the cold edge of the SAF. The full SAF includes the cold peak near 3.2°C, and more, and its width is at least 220 km near the AUSSAF array.

The error bars on the mean velocity profile in ([Fig. 6](#) ) are standard errors using the number of independent crossings of the front over the array as the number of degrees of freedom. The temperature time series of ([Fig. 2](#) ) show that only at the beginning and end of the time series is the SAF clearly out of the array. For the remainder of the time series (65%) the SAF is constantly moving over the array, remaining north or south of it only briefly. We can, nevertheless, identify 10 independent crossing events from three of the moorings, although brief reversals (no more than 2–3 days) in the otherwise monotonic change in temperature are sometimes included so that as much as possible of the front is sampled. Even so, the edges of the front are sampled less often than the core (by a factor of 2). Thus, the error bars shown in [Fig. 6](#)  are the standard deviation of velocity in each bin normalized by $(df)^{1/2}$, where the number of degrees of freedom is $df = 10$ everywhere except at the outer edges of the stream where sampling is more sparse (shaded region, fewer than 25 observations) and we downgrade df to 5. The unshaded temperature bins contain a minimum of 32 and an average of 53 observations each.

An alternative method of determining the number of degrees of freedom uses integral timescales calculated from the data ([PR](#)). At 780 dbar, the integral timescale for alongstream velocity is approximately 25 days. Dividing this into the number of days the SAF is close to the array, 450 days, gives 20 degrees of freedom. This method would give smaller error bars and we prefer to use the more conservative estimate of 10 (5) degrees of freedom.

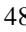
4. Mean baroclinic velocity from CTD data

a. The method

We now introduce a method to determine the mean cross-stream profile of alongstream baroclinic (geostrophic) velocity in a meandering current such as the ACC using CTD data from repeat hydrographic transects. We have used six repeats of WOCE transect SR3. For each CTD profile, the dynamic height of selected pressure surfaces relative to 3320 dbar is plotted as a function of δ_{780} ([Fig. 7](#) ). The scatter of points at each pressure level is small considering that all six transects have been included. The points lie along a set of smooth curves, indicating that the cross-stream structure of dynamic height for the ACC is relatively fixed in time. A smoothing cubic spline ([Reinsch 1967](#)) is fitted to the scatter of dynamic height as a function of δ_{780} at each pressure level, D_p , which is then differentiated with respect to cross-stream distance to obtain alongstream baroclinic velocity as a function of cross-stream distance

$$v_{bc}(p, y) = \frac{-1}{f} \frac{\Delta D_p(y)}{\Delta y}. \quad (2)$$

The velocity estimates are sensitive to the level of detail in the spline fit; we have subjectively chosen the closeness of the fits so that the resulting velocity profiles are smooth but the primary features remain.

While only the component of geostrophic velocity normal to the SR3 line can be calculated directly from CTD data, by taking the additional step of calculating dynamic height as a function of δ_{780} , all of the alongstream baroclinic flow is captured. This additional step removes the problem of the CTD transects crossing the ACC fronts obliquely because δ_{780} gives the true cross-stream distance irrespective of the orientation of the fronts relative to the transects. Also, because dynamic height increases with increasing δ_{780} , v_{bc} according to (2) is always positive, “downstream,” and so can accommodate reversals of flow caused by meandering of the front. For example, consider a cold-core ring, several of which are seen in the SR3 sections ([Fig. 8](#) ; e.g., Jan 1994, 48.5°S). The vertical density structure is roughly identical at equal distances in any direction from the ring's center, and the alongstream baroclinic velocity is therefore the same at a given value of δ_{780} on all sides of the ring.

A limitation of this method is that the relationship between the cross-stream coordinate (δ_{780}) and cross-stream distance

must be determined from another source. Here, we are able to use $y(\delta_{780})$ from the current meters. Unfortunately, these have less spatial coverage than the CTDs and so (2) is only valid for the range of δ_{780} seen by the current meters, indicated by the y axis in [Fig. 7](#).

To compare the structure of baroclinic and absolute velocity across the SAF, to the extent possible given the different temporal sampling of the current meters and hydrography, we estimate \mathbf{v}_{bc} at the five current meter levels and at 0 and 100 dbar, referenced to the deepest current meter level (3320 dbar).

The error in baroclinic velocity includes error contributions from both the dynamic height and the cross-stream distance, and is calculated as

$$\mathbf{v}_{\text{err}}(p, y) = \frac{1}{f} \frac{\Delta D_p(y)}{\Delta y} \sqrt{\left(\frac{D_{p \text{ err}}}{\Delta D_p(y)}\right)^2 + \left(\frac{y_{\text{err}}(y)}{\Delta y}\right)^2}; \quad (3)$$

$D_{p \text{ err}}$ is the rms difference between dynamic height observations and the cubic spline fit at each pressure, divided by $(df_D)^{1/2}$, where $df_D = 6$ is the number of degrees of freedom available from the six independent CTD sections. Here y_{err} is the mean of the upper and lower errors in y as described in [section 3a](#), divided by $(df_y)^{1/2}$, where df_y is the number of data points used to estimate y in each δ_{780} bin ([Fig. 3](#)).

b. Mean baroclinic velocity profile

[Figure 9](#) shows the mean profile of alongstream baroclinic velocity at six levels, determined by differentiating the dynamic height curves in steps of $\delta_{780} = 0.02 \times 10^{-6} \text{ m}^3 \text{ kg}^{-1}$. There is one broad, main peak centered on $T_{780} = 5.2^\circ\text{C}$, extending from 7.2° to 4.2°C , which has a maximum velocity of 34 cm s^{-1} at 420 dbar. Two smaller peaks on the cold side of the main peak, near 3.7° and 3.2°C , reach speeds of 25 and 22 cm s^{-1} , respectively. A much weaker peak (15 cm s^{-1} at 420 dbar) is found on the warm side near 7.6°C . Each of these peaks extends to 2240 dbar and possibly deeper. The peak at the cold edge near 3.2°C is swamped by large errors, mainly in y , and is therefore not statistically significant.

Toward the northern end of the SR3 section, T_{780} and δ_{780} become unreliable indicators of cross-stream position. As seen in [Fig. 8](#), beyond the northern edge of the SAF (strong flow near 50° – 51°S) T_{780} reaches a local maximum and then decreases to the north. Associated with this temperature decrease is westward flow. To prevent this westward flow (with δ_{780} signature identical to parts of the SAF) from biasing low the stream coordinate mean profile, we have excluded all CTDs north of the flow reversal north of the SAF from the dynamic height curves and thus from the mean profile.

c. Identification of velocity peaks

The baroclinic velocity profile ([Fig. 9](#)) is structurally very similar to the absolute velocity profile ([Fig. 6](#)). Both exhibit peaks at the same cross-stream location. However, the temporal resolution in the hydrographic and current meter datasets are vastly different: six snapshots over five years compared with close to two years of continuous sampling, and only three transects (3/93, 1/94, and 1/95) were made during the deployment period of the current meters. We do not suggest that the difference between the two profiles represents the barotropic flow.

[Rintoul and Sokolov \(2001\)](#) identify two current cores north of the SAF: an anticyclonic recirculation of subantarctic zone (SAZ) water whose southern limb merges with the SAF; and a westward outflow of Tasman Sea water. If the SAZ recirculation has been sampled by the current meters, it cannot be isolated from the SAF flow in the mean absolute velocity profile and we have not attempted to exclude it from the mean baroclinic velocity profile. The Tasman Sea outflow is too far north (near 45°S) to have been sampled by the current meters and has been excluded from the mean baroclinic profile since it is north of the flow reversal north of the SAF. The flow reversal marks the center of the SAZ recirculation and thus the full strength of the recirculation is captured by the CTDs south of the reversal. Converting from δ_{780} to y as the cross-stream coordinate, though, some of the recirculation is lost since the northernmost value of y corresponds to a δ_{780} value of $1.28 \times 10^{-6} \text{ m}^3 \text{ kg}^{-1}$ and in the center of the recirculation δ_{780} exceeds this value for three of the CTD sections (10/91, 1/95, and 9/96) by up to $0.03 \times 10^{-6} \text{ m}^3 \text{ kg}^{-1}$. Thus, most but not all of the SAZ recirculation is included in the mean profiles.

On the cold side of the SAF, the Polar Front is the only current core that may have δ_{780} values high enough to be included in the mean profile. There are two branches to the Polar Front at the longitude of the SR3 section ([Rintoul and Sokolov 2001](#); SR01). The northern branch, identified by the most northern extent of the 2°C isotherm near 200 m, can be seen in [Fig. 10](#). At the Polar Front T_{780} in this section is approximately 2.45°C and the maximum T_{780} in the Polar Front

in any of the six sections is 2.56°C. This is colder than the cold edge of the mean velocity profile of [Fig. 9](#), near $T_{780} = 2.9^\circ\text{C}$. Thus, no part of the Polar Front is represented in the mean velocity profile.

We therefore interpret the four velocity peaks in both mean profiles ([Fig. 6](#) and [Fig. 9](#)) to be jets of the SAF with some of the eastward component of the SAZ recirculation also included.

d. Streamwise mean versus geographic mean

In the case of absolute velocity measurements from a current meter array of limited spatial extent in the vicinity of a meandering stream, it is clear that one can only obtain a time-averaged cross-stream profile of velocity along the stream by the use of a streamwise averaging technique. In the case of baroclinic velocity calculated from CTD data crossing the stream there is more than one approach available. The flow across the transect can be calculated from the geostrophic relation. If the transect is repeated then a time average may be obtained by averaging the velocity sections in geographic coordinates. The following will demonstrate the shortcomings of this approach when the CTD transect crosses a meandering stream.

Geostrophic velocity calculations are only able to capture the component of flow that is normal to the hydrographic section. An illustration of undersampling by hydrography of the velocity of a meandering stream is given in [Fig. 11](#). Geostrophic velocity normal to the SR3 section at 100 dbar is plotted against ADCP velocity at 100.6 m (averaged between station pairs) for the three most recent transects. The ADCP velocities shown are technically speeds, but negative indicates a westward component is present. Geostrophic velocity is calculated relative to the deepest common level of station pairs.

Geostrophic velocities are for the most part lower than ADCP velocities, with points lying below (above) the one-to-one line for velocity greater (less) than zero. Of course, we expect the ADCP velocity to differ from the geostrophic velocity since the ADCP measures absolute (baroclinic + barotropic) velocity. In addition, the ADCP measures both the cross-section and along-section components of velocity, while only the former can be inferred from geostrophic calculations using CTD stations. When the geostrophic velocity is substantially smaller than the ADCP velocity, however, this suggests that the CTD transect crosses the SAF obliquely, missing a large portion of the geostrophic flow. The largest difference between CTD station pair and ADCP velocity is 20–40 cm s^{-1} during July 1995 (cluster of circles where ADCP velocity is approximately 40 cm s^{-1}). These points are from CTDs north of 50°S.

A map of sea surface height, concurrent with the July 1995 CTD transect, indicates the presence of a cyclonic circulation north of the strongest flow whose westernmost edge grazes the SR3 section near 48°S ([Fig. 12](#)). This implies flow northward along the SR3 line from 49° to 47°S, which is corroborated by the ADCP velocities at 100 m (vectors in [Fig. 12](#)). The low geostrophic velocities from CTD data that we see for this transect are therefore a result of the SAF flowing along rather than across the section. Note that while a CTD section that crosses a front obliquely will underestimate the peak velocities and make the front look broader, it will give the same total transport as an orthogonal section. [The sea surface height map was constructed by adding sea surface height anomalies from the TOPEX/Poseidon, *ERS-1*, and *ERS-2* satellite altimeters ([Le Traon et al. 1998](#)) to the surface dynamic height from the [Olbers et al. \(1992\)](#) climatology.]

In addition to the problem of individual transects underestimating the alongstream flow of the current, averaging repeat transects can be problematic for a current whose position changes in time. [Figure 13a](#) shows geostrophic velocity of the sea surface relative to 2240 dbar for the six occupations of SR3, and their geographic mean, as a function of distance from the northern branch of the SAF. Distance has been calculated assuming the transects are meridional. The latitudes of the northern branch of the SAF, identified by [SR01](#), are 50.4°S, 50.5°S, 50.9°S, 50.2°S, 50.3°S, and 50.9°S for the transects in October 1991, March 93, January 94, January 95, July 95, and September 96, respectively. A reference level of 2240 dbar was used for [Figs. 13a,b](#) because the deeper current meter level (3320 dbar) is deeper than some parts of the topography on this section.

The northern SAF is aligned in [Fig. 13a](#), but the other fronts are not, since the fronts move laterally relative to one another in geographic space ([SR01](#)). For example, the gentle peak in velocity in the geographic mean near –200 km is composed of flows ranging from strong peaks in 1995 and 1996, to a strong trough in 1994. The misaligned curves result in a broad and weakened peak in mean velocity. The streamwise profile does not suffer the smearing evident in the geographic mean since the fronts are relatively fixed in δ_{780} space, as shown by the tight relationship between dynamic height and δ_{780} in [Fig. 7](#).

[Figure 13b](#) compares the geographic mean of [Fig. 13a](#) (dashed line), and the mean streamwise profile of baroclinic velocity (solid line), both are surface velocity relative to 2240 dbar. The geographic mean has been shifted so that the strongest velocity is coincident with the strongest velocity in the streamwise mean. Note that for the geographic mean, distance is a displacement from the location of the northern branch of the SAF and is calculated from the CTD station positions. While for the streamwise mean, distance is the cross-stream coordinate $y(\delta_{780})$ determined in [section 3a](#), which is tied to the density structure of the current.

The streamwise mean and the geographic mean have similar peak velocities, which is not surprising since the geographic averaging was done after aligning the northern branch of the SAF, which forms the strongest peak in the mean. The streamwise mean is slightly weaker due to the smoothing applied to the streamwise dynamic height curves before

differentiating to obtain streamwise baroclinic velocity; we could adjust the cubic spline fit to increase velocity at the peak. The width of the main peak is also similar in both means. Away from the main peak, though, the geographic mean velocities fall off much more quickly than for the streamwise mean.

Figure 13c shows the streamwise (pluses) and geographic (dots) y coordinates plotted as a function of the dynamic height of the sea surface relative to 3320 dbar. The extremely small scatter of the streamwise points is in itself a convincing argument for the streamwise approach. Close to the main jet ($y = -30$ km), the two coordinates give similar distances for a given dynamic height value. Away from this central region, the geographic distances are much larger (up to 50/150 km for negative/positive values of y), resulting in a stretched velocity curve compared with the streamwise mean. More importantly, the large scatter in geographic y versus dynamic height (Fig. 13c) means that velocities with the same y values can be associated with very different points in the current's density field, and their geographic mean will smear the cross-stream structure of the current. Thus, the low geographic mean velocities on the flanks of the main peak are a combination of undersampling due to nonorthogonal sections, and of using a coordinate system detached from the density structure of the current.

5. Transport structure

The absolute volume transport of the SAF can be estimated from the mean absolute alongstream velocity profile in Fig. 6. First, velocity must be extrapolated from the current meter levels to the sea surface and bottom. Based on vertical profiles of geostrophic shear from SR3 CTDs, we set bottom velocity equal to the velocity at the deepest instrument since the vertical shear below 3320 dbar is small. We used Hall's (1986) extrapolation method to extend current meter velocities to the sea surface, producing shear profiles that compare well with geostrophic shear from the CTD data. Specifically, velocity at 100 dbar is assumed to be $\mathbf{v}_1 = \mathbf{v}_4 + 0.5 \times (\mathbf{v}_4 - \mathbf{v}_7)$, where \mathbf{v}_4 and \mathbf{v}_7 are velocities at $P_4 = 420$ dbar and $P_7 = 780$ dbar, respectively. Velocity at the sea surface is assumed equal to the velocity at 100 dbar.

Volume transport is then calculated for each cell, bounded by the vertical levels at which we know velocity and by the cross-stream bins. The transport within each cell is the mean of velocity at the four corners of the cell multiplied by the height of the cell and by the width of the bin. The total transport is simply the sum of transport in component cells $T(j, i)$, where subscript j represents the cell level and i represents the bin number. The error in the transport for each cell is calculated as

$$T_{\text{err}}(j, i) = T(j, i) \sqrt{\left(\frac{\overline{\mathbf{v}_{\text{err}}}(j, i)}{\overline{\mathbf{v}}(j, i)}\right)^2 + \left(\frac{\sqrt{y_{\text{err}}(i)^2 + y_{\text{err}}(i+1)^2}}{y(i+1) - y(i)}\right)^2}, \quad (4)$$

where the mean velocity error for each cell, $\overline{\mathbf{v}_{\text{err}}}(j, i)$, is the root mean sum of squares of the velocity errors at each of the four corners of the cell, $\mathbf{v}(j, i)$ is the mean velocity of the cell, $y(i)$ is the cross-stream distance at the center of bin i , and $y_{\text{err}}(i)$ is the mean of the upper and lower errors in y at bin i as described in section 3a, normalized by $(N)^{1/2}$, for N equal to the number of data points used to estimate y in each δ_{780} bin. The total transport error is then the square root of the sum of squares of the cellwise transport errors.

In addition to absolute transport, we can estimate the baroclinic part of the transport from the absolute velocity profile. This requires the definition of the depth-independent, or barotropic, transport, which has often been defined as the near-bottom velocity times the water depth. For the AUSSAF data, the structure of alongstream velocity is quite different at the deepest level (3320 dbar) compared with the shallower levels and fluctuates on shorter timescales (PR). There is also a deep counterflow on the warm side at $y > 25$ km and a deep intensification of eastward flow from -140 to -80 km (Fig. 6), neither seen at shallower levels. In contrast, velocities at 2240 dbar are highly coherent with velocity at shallower levels and are clearly the deep expression of the shallow velocities.

We therefore compare two alternative definitions of barotropic transport: $u_{2240} \times H$ and $u_{3320} \times H$ (for water depth $H = 3800$ m). The latter definition provides an estimate of how much transport is missed by geostrophic calculations relative to a deep level, as is usually assumed for the SAF. Figure 14 shows the cross-stream profile of absolute transport \mathcal{T} , and the cross-stream profiles of baroclinic transport BC_{2240} , defined as $(\mathcal{T} - u_{2240} \times H)$, and BC_{3320} , defined as $(\mathcal{T} - u_{3320} \times H)$. Integrating the transport curves across the stream gives estimates of total volume transport (Table 2).

Barotropic transport per unit width for the shallow definition $(\mathcal{T} - \text{BC}_{2240})$ is relatively uniform across the SAF, although it is amplified at positions where there are peaks in absolute velocity. The range of barotropic transport is $100\text{--}320 \text{ m}^2 \text{ s}^{-1}$ (equivalent to $2.6\text{--}8.4 \text{ cm s}^{-1}$ barotropic velocity). For the deep definition $(\mathcal{T} - \text{BC}_{3320})$, the barotropic transport varies considerably across the stream: $100 \text{ m}^2 \text{ s}^{-1}$ (2.6 cm s^{-1}) in the core; $25\text{--}225 \text{ m}^2 \text{ s}^{-1}$ ($0.7\text{--}5.9 \text{ cm s}^{-1}$) on the cold side; and approximately $50 \text{ m}^2 \text{ s}^{-1}$ (1.3 cm s^{-1}) westward on the warm side. Both of these representations of the barotropic transport

structure are equally valid and serve to illustrate the sensitivity to the definition of the barotropic flow.

The integrated barotropic transports are $BT_{2240} = 50$ Sv and $BT_{3320} = 16$ Sv for the 2240 dbar and 3320 dbar definitions, respectively. We estimate that transport relative to the bottom captures 86% of the absolute transport of the SAF ($=BC_{3320}/T$).

[Rintoul and Sokolov \(2001\)](#) found that the mean baroclinic transport of the SAF south of Australia is 105 ± 7 Sv. (In their study, the limits of the SAF were operationally defined to extend from the southern limit of the SAZ recirculation to the transport minimum found between the SAF and the PF.) They used the same six repeat hydrographic sections that we have used in this analysis, referenced to the deepest common level of CTD pairs. Their estimate is close to our estimate of baroclinic transport from current meters (BC_{3320} , 100 ± 12 Sv), but as discussed in [section 4c](#), the average of six snapshots should not be compared with the average of a 2-yr time series. The obvious quantity to compare with [Rintoul and Sokolov's \(2001\)](#) estimate is the baroclinic transport from the streamwise mean baroclinic velocity profile since both quantities are derived from the same data using different methods. The baroclinic transport estimated from the mean baroclinic velocity profile relative to 3320 dbar is 74 ± 4 Sv, 31 Sv smaller than Rintoul and Sokolov's value relative to the bottom.

The geostrophic shear between 3320 dbar and the bottom results in a baroclinic transport of 3.3 to 5.8 Sv over the six transects, using the same CTD pairs defined by [Rintoul and Sokolov \(2001\)](#) to be in the SAF, which is not large enough to account for the missing transport.

The CTDs defined to be in the SAF by [Rintoul and Sokolov \(2001\)](#) extend into waters with T_{780} values 0.6°C colder than seen in our mean profiles, to 2.3°C compared with 2.9°C . This strongly suggests that our mean profiles are missing part of the SAF's cold edge, as is also suggested by the large transports per unit width at the cutoff on the cold side in [Fig. 14](#). The transports at the cutoff on the warm side are also relatively large. From [section 4b](#) we know that the missing warm-side tail is that of the SAZ recirculation. We are confident that all of the warm side of the SAF itself has been sampled, although it is difficult to distinguish from the SAZ recirculation.

We recalculated integrated geostrophic transport between the surface and 3320 dbar relative to 3320 dbar for the six CTD sections, this time including only those CTDs whose T_{780} value falls within the range of the streamwise mean profile, and obtained 64.7 ± 11.7 Sv. This number is closer to the transport from the streamwise mean but still leaves about 9 Sv unaccounted for, a discrepancy smaller than the error in the transport. Thus, for the same range in T_{780} values (same CTD profiles) the streamwise estimate of mean baroclinic transport relative to 3320 dbar is consistent with 0/3320 dbar geostrophic transport from the six sections, within the error bars.

To estimate how much SAF transport is missed by the streamwise mean profiles, we calculate integrated transport relative to the bottom for the six CTD transects within the T_{780} range of the mean profiles ($=68.6 \pm 12$ Sv), and compare this to [Rintoul and Sokolov's \(2001\)](#) estimate. We conclude that the mean profiles miss approximately 35% ($= [105 - 68.6]/105$) of the SAF transport due to not sampling all of the cold side. Part of this loss may be compensated by an overestimate of SAF transport of close to 15% due to the inclusion of the SAZ recirculation in the mean velocity profiles ([section 4b](#)) since [Rintoul and Sokolov \(2001\)](#) estimated the mean baroclinic transport of the SAZ and the SAF, averaged over the six transects, to be 22 ± 8 Sv and 105 ± 7 Sv, respectively. Thus, we suggest that 116 Sv is a conservative estimate of the mean absolute transport of the SAF south of Australia.

In summary, the SAF transport south of Australia is predominantly baroclinic with only 14% not accounted for by geostrophic calculations relative to the bottom. The cross-stream structure of the barotropic transport varies according to the reference level used to define it, but in both definitions discussed above, the barotropic transport is strongest at the cross-stream locations of peaks in absolute velocity.

6. Linear instability analysis

Our profile of alongstream velocity as a function of cross-stream distance provides the opportunity to estimate the cross-stream derivative of velocity. The profiles of $u(y)$ in [Fig. 6](#) are not smooth enough to calculate a continuous horizontal gradient, so we fit a smoothing cubic spline ([Reinsch 1967](#)) to them before calculating $\partial u/\partial y$ ([Fig. 15b](#)). [Figure 15a](#) shows $f^{-1}\partial u/\partial y$ at 420 dbar, the depth at which the largest values are found. This Rossby number reaches a maximum of 0.06, verifying that the geostrophic approximation is valid for the mean flow at this location.

The second derivative of u with respect to y allows the barotropic stability of the flow to be assessed. A necessary condition for barotropic instability (or release of energy from the mean velocity field by horizontal Reynolds stresses) to occur is that $\beta - u_{yy}$ be less than zero ([Gill 1982](#)), where $\beta = \partial f/\partial y$. In [Fig. 15b](#), the heavy lines over the smoothed velocity profiles show where this condition is satisfied. [Peterson et al. \(1982\)](#) made a similar calculation for Drake Passage baroclinic velocities estimated from one hydrographic section and also found that the instability criterion was met on the flanks of the velocity peaks. Reynolds stresses at the AUSSAF array have been shown to be small ([PR](#)) and, while we have shown that the necessary condition for barotropic instability is satisfied, the amount of energy extracted from the mean flow in this manner is also small ([PR](#)).

One way for the necessary condition for baroclinic instability to be satisfied is for the meridional (here cross-stream) gradient of potential vorticity,

$$Q_y = \beta - f^2 \left(\frac{U_z}{N^2} \right)_z \quad (5)$$

to change sign within the fluid ([Gill et al. 1974](#)).

We estimate Q_y from the SR3 hydrographic data as follows:

- select all CTDs that lie within the SAF as defined by [Rintoul and Sokolov \(2001\)](#)
- calculate mean profiles of temperature, salinity, and geostrophic velocity from the selected CTDs
- calculate U_z and N^2 from the mean profiles
- smooth U_z and N^2 using a second-order Butterworth filter with a half-power roll-off of 40 m, passed both ways to eliminate the introduction of phase lags
- calculate Q_y from smoothed U_z and N^2 .

[Figures 15c–e](#) show the smoothed U_z , smoothed N^2 , and Q_y . Above 175 m, the smoothed profile does not well represent the sharp decrease of N^2 toward the surface. Below 3000 m, the topography begins to reduce the number of profiles that reach this level, and mean U_z and N^2 become more noisy. We therefore do not calculate Q_y above 175 m or below 3000 m, and do not examine the remaining baroclinic instability criteria ([Gill et al. 1974](#); [Wright 1981](#)), which are determined by surface and bottom conditions.

Here Q_y is very sensitive to the shape of U_z and N^2 and we focus only on the strongest zero crossing, near 560 m. The features in the U_z and N^2 profiles that combine to make this strong crossing are strong vertical shear and the change in sign of N_z^2 in the negative slope region of N^2 . The strong vertical shear near 560 m is a consistent feature of all 62 velocity profiles included in the mean. The negative slope of mean N^2 between 300 and 800 m is a feature of 63% of the individual profiles. We are, therefore, confident in interpreting the zero crossing of Q_y near 560 m to mean that the necessary condition for baroclinic instability is satisfied in the SAF.

7. Discussion

a. Velocity

In this section we compare our cross-stream profile of mean absolute velocity to the few observations of absolute velocity made in the ACC. Most prior measurements of velocity in the SAF are from Drake Passage. Numerous hydrographic transects have provided information on the baroclinic field in Drake Passage, and in three cases ([Whitworth et al. 1982](#)) concurrent current meter measurements have provided a reference level velocity enabling instantaneous absolute velocity across the passage to be determined. More recently, [Donohue et al. \(2001\)](#) have measured absolute velocity in the SAF in the Pacific Ocean normal to six WOCE hydrographic lines (between 88°W and 173°E), using shipboard acoustic Doppler profiler measurements to reference the geostrophic velocities.

The streamwise mean absolute velocity at AUSSAF has a peak of $51.9 \pm 4.3 \text{ cm s}^{-1}$ at 420 dbar. Instantaneous velocities (40-h low passed) at that depth reached 73 cm s^{-1} during crossings of the SAF. At 2240 dbar, the peak mean velocity was $8.4 \pm 0.9 \text{ cm s}^{-1}$ and the maximum instantaneous velocity during the two-year deployment was approximately 20 cm s^{-1} .

In Drake Passage, peak absolute speeds in the SAF (from hydrographic sections referenced to direct velocity measurements) range from 45 to 75 cm s^{-1} at the sea surface and 25 to 55 cm s^{-1} at 500 m ([Nowlin et al. 1977](#); [Whitworth et al. 1982](#)). A time series of velocity at 2770 m in the SAF at Drake Passage, from mooring 2 of the FDRAKE 79 experiment ([Pillsbury et al. 1979](#)), shows that speeds of 40 cm s^{-1} are reached several times during the 1-yr record. [Donohue et al.'s \(2001\)](#) ten estimates of SAF speed at the sea surface in the south Pacific are lower than in Drake Passage, 22.3–53.0 cm s^{-1} , with a mean of 37.5 cm s^{-1} .

Clearly, the strength of the SAF changes in time and it is difficult to draw conclusions from the variations between the three locations where absolute velocities in the SAF have been measured. The above suggests that peak velocities near 500 m are greater south of Australia than in Drake Passage. The vertical shear south of Australia is also greater than in Drake Passage so that by deep levels (>2000 m) peak velocities in Drake Passage exceed AUSSAF peak values. In the less constrained South Pacific the velocity in the SAF is considerably lower. Other evidence also suggests the ACC is more diffuse in the South Pacific [e.g., climatological dynamic height (Olbers et al. 1992), and altimeter observations and models (Wilkin and Morrow 1994)].

The width of the SAF in the mean profile is 220 km. The true width is probably slightly greater since some of the cold side of the SAF has been excluded from the mean profile. Nowlin and Clifford (1982) estimated the width of the SAF in Drake Passage ranged from 40 to 83 km, based on water property distributions from six hydrographic transects. This is substantially narrower than our estimate south of Australia and reflects the difference in defining the limits of a front based on property distributions compared with using velocity. A vertical section of relative geostrophic speed from one of the Drake Passage transects considered by Nowlin and Clifford (1982) suggests a SAF width of approximately 160 km. We note here that the SAF south of Australia is composed of several branches. Such filamented structure has not been documented for the SAF at other longitudes.

The method described in section 4a for obtaining a mean cross-stream profile of alongstream baroclinic velocity from hydrographic data has two advantages over estimating mean geostrophic velocity from station pairs. First, from station pairs, only the velocity normal to the section can be calculated. The streamwise profiling method allows the full alongstream flow to be determined, regardless of the angle at which the section crosses the front. Second, the movement of the fronts relative to one another that we see in a geographic coordinate frame does not blur the streamwise mean because the stream coordinate is tied to the density structure of the current. The streamwise average gives a synoptic view of the front with a realistic estimate of the width and speed of the front, averaged only in time. A limitation to the portability of this profiling method to other hydrographic lines is that the relationship between cross-stream distance and δ_{780} (or some equivalent quantity estimated from hydrographic data) must be known. Here we used a relationship determined from current meter data. Satellite altimeter observations, linked with dynamic height from the CTDs, may provide an alternative. Assuming such a method would work, the baroclinic profiling technique will allow more information on the velocity field to be determined from hydrographic lines than has hitherto been possible.

b. Transport

The mean absolute volume transport of the SAF south of Australia, 116 ± 10 Sv, is a large proportion of the mean absolute transport through Drake Passage, 134 ± 13 Sv (Whitworth and Peterson 1985). In section 5, we suggested that our estimate of absolute transport was a conservative one; thus the mean transport of the SAF south of Australia represents at least 83% of the total mean ACC flow through Drake Passage. While this figure is high, it is given some support by Rintoul and Sokolov (2001), who found that for the baroclinic field the SAF south of Australia carries about 71% of the total ACC flow. The northern and southern branches of the Polar Front, combined, carry 18% of the total baroclinic transport south of Australia. Rintoul and Sokolov (2001) have shown that there is significant westward baroclinic flow at SR3 (~ 40 Sv), north and south of the ACC, and the eastward flow must be larger than at other longitudes to compensate.

Yaremchuk et al. (2001) have used a least squares dynamically constrained optimization technique to estimate absolute transport across the SR3 section. They find that the mean transport of the SAF together with the eastward branch of the SAZ recirculation carries 107 ± 25 Sv. This is 71% of their total eastward transport of 151 ± 50 Sv, and is comparable to our estimate of 116 ± 10 Sv. They also find significant westward absolute flows north and south of the SAF, which in total amount to approximately 15 Sv.

At Drake Passage, the SAF contribution to the total baroclinic flow is much less than that at the SR3 section. Nowlin and Clifford (1982), averaging six XBT and STD transects across Drake Passage, found that 31.5% of the total baroclinic flow through Drake Passage is carried by the SAF. The Polar Front (PF) carries 27% and the southern ACC front [called the Continental Water Boundary in Nowlin and Clifford (1982)] carries 15.1%. The contributions by these two fronts were estimated from averages of 13 transects for the SAF and 7 transects for the PF. The remaining transport (26%) is carried by the weaker eastward flows between the fronts, indicated by gentle shoaling of isopycnals toward the south.

The low relative transport of the SAF found by Nowlin and Clifford (1982) may in part be due to their narrow front definition. Nevertheless, these results suggest that the relative transport contribution of individual fronts to the total flow of the ACC varies significantly along the circumpolar path of the current, consistent with the results of Orsi et al. (1995).

c. Stability

The linear stability analysis indicates that barotropic instability can occur on the flanks of peaks in along-stream velocity, and that baroclinic instability can also occur. The relative strengths of the two instability mechanisms have been assessed from calculations of energy conversion rates in PR. These showed that baroclinic conversion from available potential energy to eddy potential energy occurred at a rate of $10.17 \pm 11.33 (\times 10^{-4} \text{ cm}^2 \text{ s}^{-3})$, while barotropic conversion was 60 times slower, $0.16 \pm 0.94 (\times 10^{-4} \text{ cm}^2 \text{ s}^{-3})$.

In Drake Passage, baroclinic conversion was also found to be the dominant mechanism for energy exchange, here also

two orders of magnitude larger than barotropic conversion (Wright 1981). Wright concluded that in central Drake Passage the linear condition for baroclinic instability is satisfied because somewhere within the fluid Q_y is of the same sign as U_z at the bottom. We have shown that south of Australia Q_y changes sign within the fluid satisfying an alternative condition for baroclinic instability. This condition was also found to apply in Drake Passage. Both Wright (1981) and Bryden (1979) found that Q_y in Drake Passage changed sign within the fluid, but that the calculation is very sensitive to the profiles of vertical shear and buoyancy frequency.

8. Summary and conclusions

We have demonstrated the power of the streamwise profiling technique introduced by Hall and Bryden (1985) and have shown its applicability to the ACC. Measurements from a current meter array, small in spatial coverage, have been transformed into a cross-stream profile of alongstream absolute velocity in the SAF. Similarly, repeat hydrographic transects have been averaged in stream coordinates to produce a mean cross-stream profile of alongstream baroclinic velocity in the SAF.

The absolute and baroclinic velocity profiles are very similar in structure, each having one main peak between three smaller peaks at the same cross-stream positions in each profile. Each of the absolute velocity peaks extend to 3320 dbar and, since there is little vertical shear below this level, we conclude that the SAF extends to the seafloor (near 3800 m). In the main peak, the 2-yr mean absolute velocity from current meters reaches 52 cm s^{-1} at 420 dbar; the mean baroclinic velocity from six CTD sections reaches 34 cm s^{-1} . Alongstream flow is coherent at all depths within the main peak. At 3320 dbar, there is a small counterflow at the cold edge of the stream in the absolute velocity profile. The width of the SAF near the AUSSAF array is at least 220 km. The SAF is the strongest jet of the ACC south of Australia and has a mean absolute transport of at least $116 \pm 10 \text{ Sv}$ at 143°E , of which we estimate 16 Sv (14%) would be missed by geostrophic calculations relative to a deep level.

The linear conditions for baroclinic and barotropic instability are satisfied at the AUSSAF array. This is consistent with the results of PR, which showed that baroclinic conversion is the dominant mechanism by which eddies grow south of Australia, and that barotropic conversion occurs but is much weaker.

The combination of this work and PR gives a thorough description of the mean flow and eddy variability of the SAF south of Australia at the AUSSAF current meter array. This site is only the third where long-term in situ measurements of the ACC have been made. While many differences are apparent between the three sites, such as the latitude and strength of fronts and the level of eddy activity, these data suggest that the processes found to be important in Drake Passage are also important outside this unique environment.

The task of measuring the absolute transport of the ACC is a difficult one. Even at the so-called choke points, the relatively confined passages between Antarctica and the other Southern Hemisphere continents, the sections are much too long to contemplate a coherent “picket fence” of moorings to monitor the ACC transport. Direct velocity measurements from either vessel-mounted or lowered ADCPs are not yet of sufficient accuracy to provide a reference for transport estimates across long sections (Donohue et al. 2001).

While the transport estimates presented in this paper are only for the SAF, by providing a mean synoptic view of the strongest jet of the ACC south of Australia, they provide an important constraint on the transport of the entire ACC. Further progress is likely to be made by combining streamwise averages of direct velocity measurements such as those presented here and a range of other observations (shipboard and lowered ADCP, hydrographic measurements, altimetry) with dynamical constraints in inverse calculations.

Acknowledgments

We thank the officers, crew, and scientific teams on *Aurora Australis* for their contribution to the collection of the current meter and CTD data. A series of enlightening discussions with Nathan Bindoff resulted in the development of the alternative method for determining the cross-stream coordinate described in section 3a. Comments from Melinda Hall, Randolph Watts, Richard Coleman, and two anonymous reviewers led to many improvements in the manuscript. The altimeter products were produced by the CLS Space Oceanography Division as part of the European Union's Environment and Climate project AGORA (ENV4-CT9560113) and DUACS (ENV4-CT96-0357) with financial support from the Centre for Earth Observation and Midi-Pyrénées regional council. The ERS products were generated as part of the proposal A02.F105 by the European Space Agency. This work was supported in part by Environment Australia through the National Greenhouse Research Program, and by the Australian National Antarctic Research Expeditions (ANARE). HP thanks the Vetlesen Foundation for their support. This paper is a contribution to the World Ocean Circulation Experiment.

REFERENCES

Bower A. S., and N. G. Hogg, 1996: Structure of the Gulf Stream and its recirculations at 55°W . *J. Phys. Oceanogr.*, **26**, 1002–1022. [Find this article online](#)

- Bryden H. L., 1979: Poleward heat flux and conversion of available potential energy in Drake Passage. *J. Mar. Res.*, **37**, 1–22. [Find this article online](#)
- Donohue K., E. Firing, and S. Chen, 2001: Absolute geostrophic velocity within the Subantarctic Front in the Pacific Ocean. *J. Geophys. Res.*, **106**, 19869–19882, (C9). [Find this article online](#)
- Georgi D. T., and J. M. Toole, 1982: The Antarctic Circumpolar Current and the oceanic heat and freshwater budgets. *J. Mar. Res.*, **40**, 183–197, (Suppl.). [Find this article online](#)
- Gill A. E., 1982: *Atmosphere–Ocean Dynamics*. 1st ed. Academic Press, 662 pp.
- Gill A. E., J. S. Green, and A. J. Simmons, 1974: Energy partition in the large-scale ocean circulation and the production of mid-ocean eddies. *Deep-Sea Res.*, **21**, 449–528. [Find this article online](#)
- Hall M. M., 1986: Horizontal and vertical structure of the Gulf Stream velocity field at 68°W. *J. Phys. Oceanogr.*, **16**, 1814–1828. [Find this article online](#)
- Hall M. M., 1989: Velocity and transport structure of the Kuroshio Extension at 35°N 152°E. *J. Geophys. Res.*, **94**((C10)), 14445–14459. [Find this article online](#)
- Hall M. M., and H. L. Bryden, 1985: Profiling the Gulf Stream with a current meter mooring. *Geophys. Res. Lett.*, **12**, 203–206. [Find this article online](#)
- Hogg N. G., 1991: Mooring motion corrections revisited. *J. Atmos. Oceanic Technol.*, **8**, 289–295. [Find this article online](#)
- Hogg N. G., 1992: On the Gulf Stream transport between Cape Hatteras and the Grand Banks. *Deep-Sea Res.*, **39**, 1231–1246. [Find this article online](#)
- Jacobs S. S., and D. T. Georgi, 1977: Observations on the southwest Indian/Antarctic Ocean. *A Voyage of Discovery* (supplement to *Deep-Sea Research*), M. Angel, Ed., Pergamon Press, 43–84.
- Johns W. E., T. J. Shay, J. M. Bane, and D. R. Watts, 1995: Gulf Stream structure, transport and recirculation near 68°W. *J. Geophys. Res.*, **100**((C1)), 817–838. [Find this article online](#)
- Le Traon P. Y., F. Nadal, and N. Ducet, 1998: An improved mapping method of multi-satellite altimeter data. *J. Atmos. Oceanic Technol.*, **15**, 522–534. [Find this article online](#)
- Nowlin W. D., Jr., and M. Clifford, 1982: The kinematic and thermohaline zonation of the Antarctic Circumpolar Current at Drake Passage. *J. Mar. Res.*, **40**, 481–507, (Suppl.). [Find this article online](#)
- Nowlin W. D., Jr., and J. M. Klinck, 1986: The physics of the Antarctic Circumpolar Current. *Rev. Geophys.*, **24**, 469–491. [Find this article online](#)
- Nowlin W. D., Jr., T. Whitworth III, and R. D. Pillsbury, 1977: Structure and transport of the Antarctic Circumpolar Current at Drake Passage from short-term measurements. *J. Phys. Oceanogr.*, **7**, 788–802. [Find this article online](#)
- Olbers D., V. Gouretski, G. Seiß, and J. Schröter, 1992: *Hydrographic Atlas of the Southern Ocean*. Alfred Wegener Institute, 17 pp. + 82 plates.
- Orsi A. H., T. Whitworth III, and W. D. Nowlin Jr., 1995: On the meridional extent and fronts of the Antarctic Circumpolar Current. *Deep-Sea Res.*, **42**, 641–673. [Find this article online](#)
- Peterson R. G., W. D. Nowlin Jr., and T. Whitworth III, 1982: Generation and evolution of a cyclonic ring at Drake Passage in early 1979. *J. Phys. Oceanogr.*, **12**, 712–719. [Find this article online](#)
- Phillips H. E., 2000: Mean flow, eddy variability and energetics of the Subantarctic Front south of Australia. Ph.D. thesis, Institute of Antarctic and Southern Ocean Studies, University of Tasmania, 158 pp.
- Phillips H. E., and S. R. Rintoul, 2000: Eddy variability and energetics from direct current measurements in the Antarctic Circumpolar Current south of Australia. *J. Phys. Oceanogr.*, **30**, 3050–3076. [Find this article online](#)
- Pillsbury R. D., T. Whitworth III, W. D. Nowlin Jr., and F. Sciremammano Jr., 1979: Currents and temperatures as observed in Drake Passage during 1975. *J. Phys. Oceanogr.*, **9**, 469–482. [Find this article online](#)
- Read J. F., and R. T. Pollard, 1993: Structure and transport of the Antarctic Circumpolar Current and Agulhas Return Current at 40°E. *J. Geophys. Res.*, **98**((C7)), 12281–12295. [Find this article online](#)
- Reinsch C. H., 1967: Smoothing by spline functions. *Numer. Math.*, **10**, 177–183. [Find this article online](#)
- Rintoul S. R., and J. L. Bullister, 1999: A late winter hydrographic section from Tasmania to Antarctica. *Deep-Sea Res.*, **46**, 1417–1454. [Find this article online](#)

Rintoul S. R., and S. Sokolov, 2001: Baroclinic transport variability of the Antarctic Circumpolar Current south of Australia (WOCE repeat section SR3). *J. Geophys. Res.*, **106**, 2815–2832, (C2). [Find this article online](#)

Rintoul S. R., and J. A. Church, 2002: A six year record of baroclinic transport variability of the Antarctic Circumpolar Current at 140°E, derived from XBT and altimeter measurements. *J. Geophys. Res.*, in press.

Smith W. H. F., and D. T. Sandwell, 1994: Bathymetric prediction from dense satellite altimetry and sparse shipboard bathymetry. *J. Geophys. Res.*, **99**, 21803–21824. [Find this article online](#)

Sokolov S., and S. Rintoul, 2001: Structure of Southern Ocean fronts at 140°E. *J. Mar. Syst.*, in press. (Special issue on ocean fronts).

Whitworth T., III., 1983: Monitoring the transport of the Antarctic Circumpolar Current at Drake Passage. *J. Phys. Oceanogr.*, **13**, 2045–2057. [Find this article online](#)

Whitworth T., III., and R. G. Peterson, 1985: Volume transport of the Antarctic Circumpolar Current from bottom pressure measurements. *J. Phys. Oceanogr.*, **15**, 810–816. [Find this article online](#)

Whitworth T., III., W. D. Nowlin Jr., and S. J. Worley, 1982: The net transport of the Antarctic Circumpolar Current through Drake Passage. *J. Phys. Oceanogr.*, **12**, 960–971. [Find this article online](#)

Wilkin J. L., and R. A. Morrow, 1994: Eddy kinetic energy and momentum flux in the Southern Ocean: Comparison of a global eddy-resolving model with altimeter, drifter and current-meter data. *J. Geophys. Res.*, **99**((C4)), 7903–7916. [Find this article online](#)

Wright D. G., 1981: Baroclinic instability in Drake Passage. *J. Phys. Oceanogr.*, **11**, 231–246. [Find this article online](#)

Yaremchuk M., N. L. Bindoff, J. Schröter, D. Nechaev, and S. R. Rintoul, 2001: On the zonal and meridional circulation and ocean transports between Tasmania and Antarctica. *J. Geophys. Res.*, **106**((C2)), 2795–2814. [Find this article online](#)

APPENDIX

9. Mean Velocity Profile Using the Method of Hall and Bryden

We again use specific volume anomaly rather than temperature for the cross-stream coordinate, a slight modification to [Hall and Bryden's \(1985\)](#) method, for reasons explained in [section 3a](#).

Using the thermal wind equation in terms of δ ([1](#)) we plot the scatter of $\partial\delta/\partial y$ at 780 dbar versus δ_{780} and calculate the linear fits to the scatter either side of the core (Fig. 16)


$$\left. \frac{\partial\delta}{\partial y} \right|_{780} = \begin{cases} 0.0066 \times \delta_{780} - 3.5836 \times 10^{-9} & \text{for } \delta_{780} < 1.102 \times 10^{-6} \text{ m}^3 \text{ kg}^{-1} \\ -0.0181 \times \delta_{780} + 2.3594 \times 10^{-8} & \text{for } \delta_{780} > 1.102 \times 10^{-6} \text{ m}^3 \text{ kg}^{-1}. \end{cases} \quad (\text{A1})$$

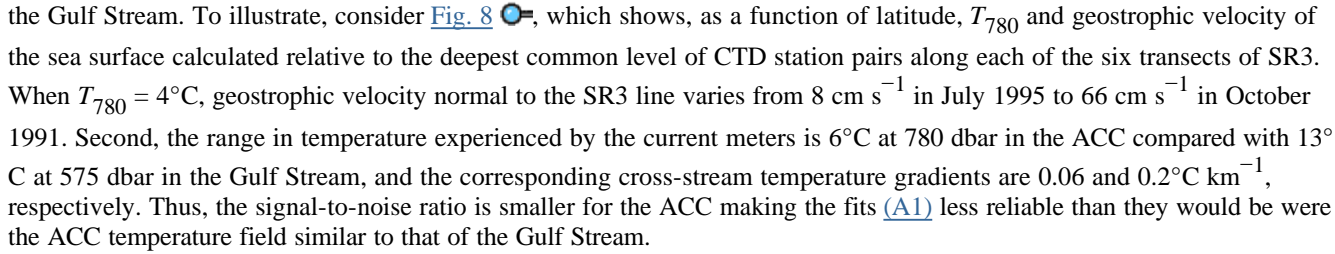
[Equations \(A1\)](#) are then inverted and integrated to obtain cross-stream distance in km,

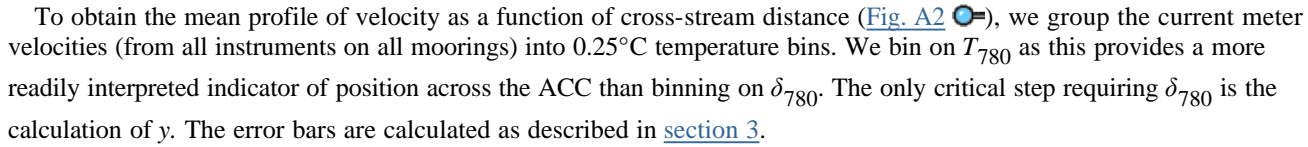
$$y(\delta_{780}) = \begin{cases} \frac{1}{0.0066} \ln\left(\frac{0.0066 \times \delta_{780} - 3.5836 \times 10^{-9}}{3.6548 \times 10^{-9}}\right) & \text{for } \delta_{780} < 1.102 \times 10^{-6} \text{ m}^3 \text{ kg}^{-1} \\ 0 & \text{for } \delta_{780} = 1.102 \times 10^{-6} \text{ m}^3 \text{ kg}^{-1} \\ \frac{-1}{0.0181} \ln\left(\frac{-0.0181 \times \delta_{780} + 2.3594 \times 10^{-8}}{3.6213 \times 10^{-9}}\right) & \text{for } \delta_{780} > 1.102 \times 10^{-6} \text{ m}^3 \text{ kg}^{-1}, \end{cases} \quad (\text{A2})$$

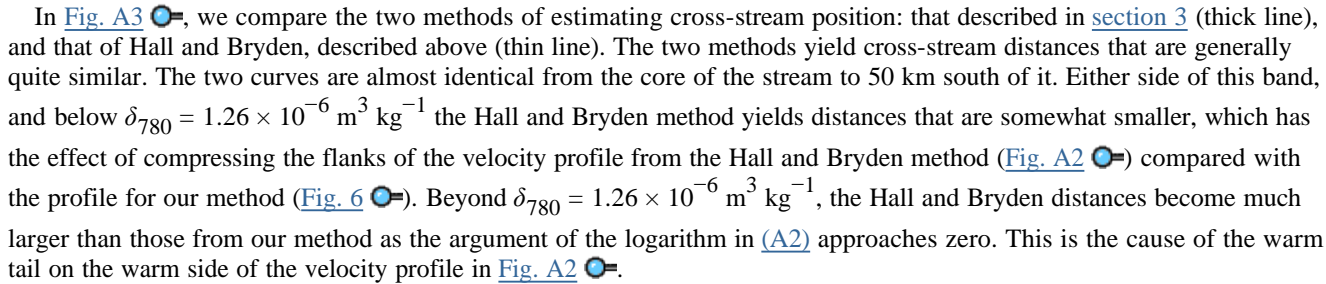
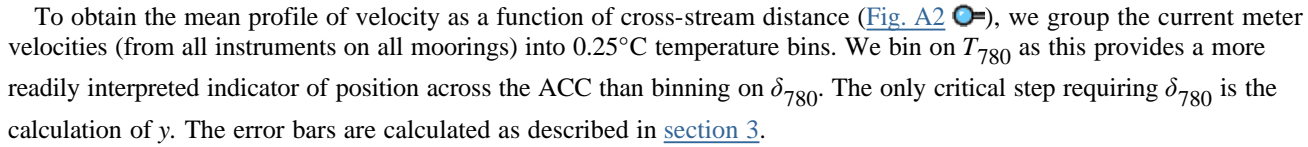
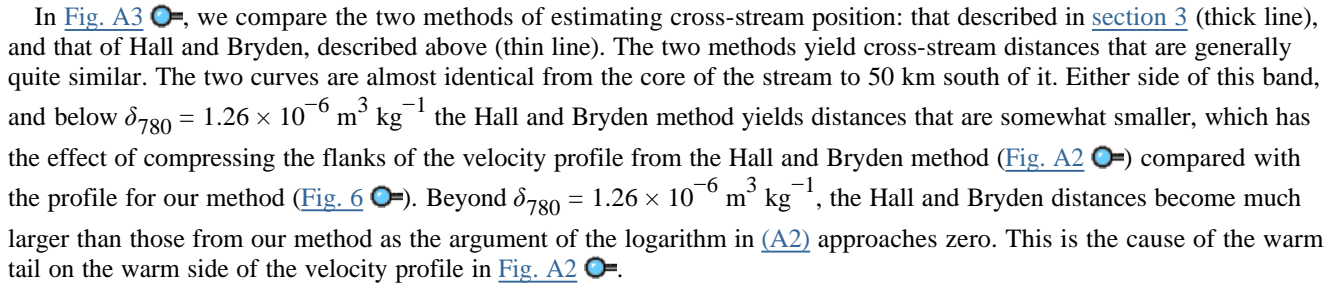
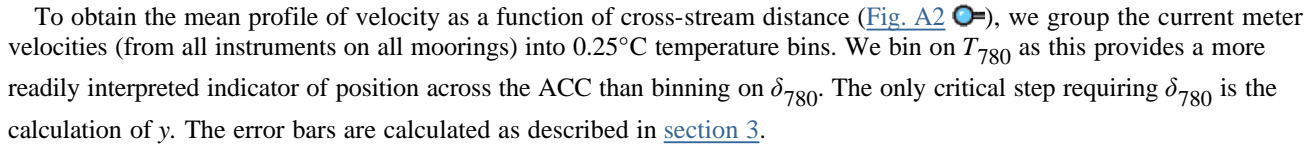
(Click the equation graphic to enlarge/reduce size)

which is shown as an alternative abscissa in Fig. 16.

The scatter in [Fig. A1](#)  is larger than in the corresponding figure of [Hall and Bryden \(1985\)](#) for two reasons. First, the cross-stream structure of the ACC is very different in nature to that of the Gulf Stream. Gulf Stream velocity decreases monotonically from a central core to its outer edges while the ACC is composed of several major fronts, the fronts themselves having regions of strong flow with weaker flow between. Therefore, in traversing the ACC from cold to warm, say, velocity does not change monotonically and for a given specific volume anomaly/temperature there is considerable variation in alongstream velocity. In other words, the cross-stream velocity profile is not so nearly “fixed” in time as it is in

of the Gulf Stream. To illustrate, consider [Fig. 8](#)  , which shows as a function of latitude, T_{780} and geostrophic velocity of the sea surface calculated relative to the deepest common level of CTD station pairs along each of the six transects of SR3. When $T_{780} = 4^\circ\text{C}$, geostrophic velocity normal to the SR3 line varies from 8 cm s^{-1} in July 1995 to 66 cm s^{-1} in October 1991. Second, the range in temperature experienced by the current meters is 6°C at 780 dbar in the ACC compared with 13°C at 575 dbar in the Gulf Stream, and the corresponding cross-stream temperature gradients are 0.06 and $0.2^\circ\text{C km}^{-1}$, respectively. Thus, the signal-to-noise ratio is smaller for the ACC making the fits [\(A1\)](#) less reliable than they would be were the ACC temperature field similar to that of the Gulf Stream.

To obtain the mean profile of velocity as a function of cross-stream distance ([Fig. A2](#) ), we group the current meter velocities (from all instruments on all moorings) into 0.25°C temperature bins. We bin on T_{780} as this provides a more readily interpreted indicator of position across the ACC than binning on δ_{780} . The only critical step requiring δ_{780} is the calculation of y . The error bars are calculated as described in [section 3](#).

In [Fig. A3](#)  , we compare the two methods of estimating cross-stream position: that described in [section 3](#) (thick line), and that of Hall and Bryden, described above (thin line). The two methods yield cross-stream distances that are generally quite similar. The two curves are almost identical from the core of the stream to 50 km south of it. Either side of this band, and below $\delta_{780} = 1.26 \times 10^{-6} \text{ m}^3 \text{ kg}^{-1}$ the Hall and Bryden method yields distances that are somewhat smaller, which has the effect of compressing the flanks of the velocity profile from the Hall and Bryden method ([Fig. A2](#) ) compared with the profile for our method ([Fig. 6](#) ). Beyond $\delta_{780} = 1.26 \times 10^{-6} \text{ m}^3 \text{ kg}^{-1}$, the Hall and Bryden distances become much larger than those from our method as the argument of the logarithm in [\(A2\)](#) approaches zero. This is the cause of the warm tail on the warm side of the velocity profile in [Fig. A2](#) .

Tables

Table 1. Dates (d/mo/yr) of operation of current meters after small gaps have been filled by mooring motion correction. Dates of occupation of WOCE SR3 hydrographic section

Pressure (dbar)	Current meter			
	West 0973.095 14256.249 E	North 09734.095 S 14270.575 E	Central 09724.75 S 14274.15 E	South 0791.545 S 14254.425 E
420	19/03-20/7/95	No data	19/03-24/1/95	18/09-12/20/94
780	19/03-20/7/95	No data	19/03-24/1/95	18/09-12/20/94
1120	19/03-23/1/95	19/03-20/4/94	19/03-24/1/95	18/09-12/20/94
2240	No data	19/03-20/4/94	19/03-24/1/95	18/09-12/20/94
3320	18/03-20/4/94	No data	No data	18/09-4/20/94

Mooring	Dates on SR3		ADCP available
	Start	End	
mo001	8/11-26/10/91	No	
mo006	1/25-26/5/93	No	
mo007	2/1-16/1/94	No	
mo008	19/1-1/2/93	Yes	
mo010	1/7-8/8/93	Yes	
mo001	30/8-21/10/96	Yes	

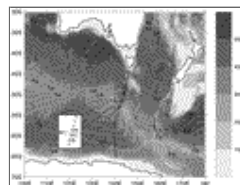
[Click on thumbnail for full-sized image.](#)

Table 2. Total volumn transport for the SAF south of Australia in Sverdrups derived from the mean absolute velocity profile ([Fig. 6](#)). Baroclinic and barotropic transports are defined relative to 2240 and 3320 dbar (see text)

	Absolute transport (Sv)	Baroclinic transport (Sv)	Barotropic transport (Sv)
\bar{T}	116 ± 10	BC ₂₂₄₀ : 66 ± 7 BC ₃₃₂₀ : 100 ± 12	BT ₂₂₄₀ : 50 BT ₃₃₂₀ : 16

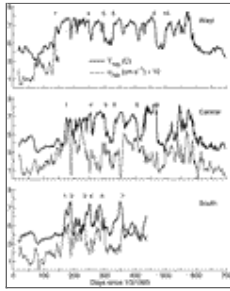
[Click on thumbnail for full-sized image.](#)

Figures



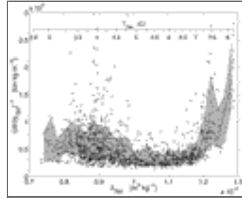
[Click on thumbnail for full-sized image.](#)

FIG. 1. Map showing location of current meters [circles identified as W(est), S(outh), C(entral), and N(orth)] and WOCE section SR3 (plus signs) overlaid on background shading of [Smith and Sandwell \(1994\)](#) bathymetry, and contours of 0–2000 dbar dynamic height (dyn m) from [Olbers et al. \(1992\)](#)



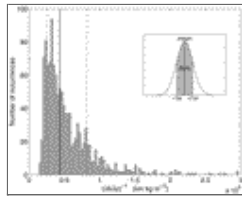
[Click on thumbnail for full-sized image.](#)

FIG. 2. Time series of temperature at 780 dbar (thick line) and alongstream velocity at 780 dbar in units of 10 cm s^{-1} (thin line) on the West, Central, and South moorings. Ten crossing events are marked



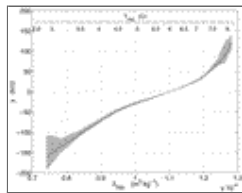
[Click on thumbnail for full-sized image.](#)

FIG. 3. Scatter of the inverse of cross-stream gradient of specific volume anomaly at 780 dbar vs specific volume anomaly at 780 dbar. Solid line is median in each svan bin, limits of shaded region are the 16th and 84th percentiles in each svan bin. Alternative abscissa: temperature at 780 dbar



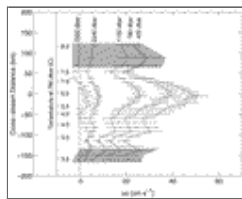
[Click on thumbnail for full-sized image.](#)

FIG. 4. Distribution of the inverse of cross-stream gradient of specific volume anomaly at 780 dbar with 16th, 50th (solid line), and 84th percentiles indicated. Inset shows that for a Gaussian distribution, ± 1 standard deviation encloses 68% of the total area under the curve



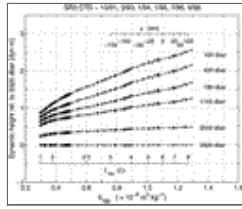
[Click on thumbnail for full-sized image.](#)

FIG. 5. Cross-stream distance y as a function of specific volume anomaly at 780 dbar. Shaded region is an estimate of the error in y corresponding to the 16th and 84th percentiles of the distribution of the inverse of cross-stream gradient of specific volume anomaly at 780 dbar. Alternative abscissa: temperature at 780 dbar



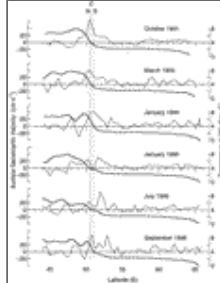
[Click on thumbnail for full-sized image.](#)

FIG. 6. Cross-stream profile of alongstream absolute (baroclinic + barotropic) velocity. Standard error is calculated for 10 (5) degrees of freedom in unshaded (shaded) bins



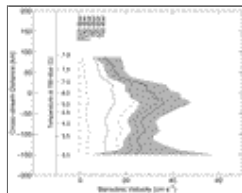
[Click on thumbnail for full-sized image.](#)

FIG. 7. Dynamic height calculated from the six CTD transects relative to 3320 dbar at each of the current meter levels and 100 dbar vs specific volume anomaly at 780 dbar. Smoothing cubic spline fits to each curve are also shown. Alternative abscissae: temperature at 780 dbar and cross-stream distance



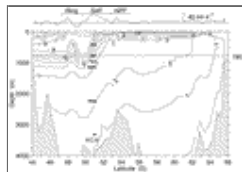
[Click on thumbnail for full-sized image.](#)

FIG. 8. Geostrophic velocity of the sea surface relative to the deepest common level of CTD pairs (thin line), and temperature at 780 dbar (thick line) along six transects of WOCE section SR3 from Tasmania (left) to Antarctica (right). Vertical lines mark positions of North, Central, and South current meter moorings



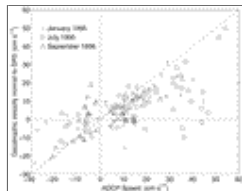
[Click on thumbnail for full-sized image.](#)

FIG. 9. Cross-stream profile of alongstream baroclinic velocity calculated using 0–3320 dbar dynamic height along SR3 and the cross-stream coordinate, $y(\delta_{780})$, determined from current meter data. Shading is an error estimate for the 100-dbar velocity



[Click on thumbnail for full-sized image.](#)

FIG. 10. SR3 temperature section for Jan 1994 and corresponding surface geostrophic velocity referenced to the deepest common level of CTD pairs. Locations of the Subantarctic Front, North Polar Front, and a cold core ring are indicated



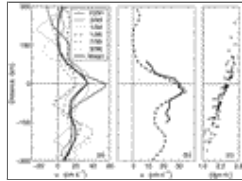
[Click on thumbnail for full-sized image.](#)

FIG. 11. Comparison of ADCP velocity at 100.6 m (positive indicates no westward component) and cross-SR3 geostrophic velocity from CTD pairs relative to the deepest common level of the pair for the latter three transects. Dashed line indicates one-to-one correspondence



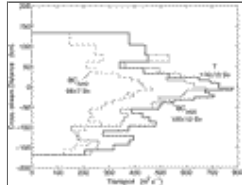
Click on thumbnail for full-sized image.

FIG. 12. Sea surface height anomalies from the *TOPEX/Poseidon*, *ERS-1*, and *ERS-2* satellite altimeters, merged and mapped onto a 0.25° grid [the CLS “MSLA” dataset ([Le Traon et al. 1998](#))], have been added to the 0–2500 dbar dynamic height from the [Olbers et al. \(1992\)](#) climatology. The sea surface height map (dyn cm) is concurrent with the Jul 1995 CTD section along SR3, for which ADCP velocities at 100.6 m are shown



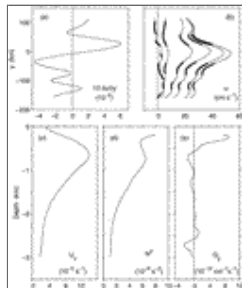
Click on thumbnail for full-sized image.

FIG. 13. (a) Geostrophic velocity of the sea surface relative to 2240 dbar from CTD pairs along six transects of SR3, and the mean, as a function of distance from the northern branch of the SAF (see text). (b) Solid line is streamwise mean baroclinic velocity relative to 2240 dbar, dashed line is mean geostrophic velocity from (a) shifted so that peak velocity is aligned with the streamwise mean peak. (c) Distance coordinate for the geographic mean (pluses) and streamwise mean (dots) vs dynamic height of the sea surface relative to 3320 dbar



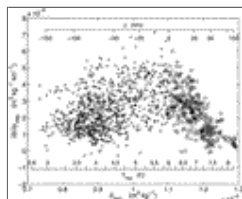
Click on thumbnail for full-sized image.

FIG. 14. Structure of volume transport per unit width of the ACC: \mathcal{T} (heavy line) is absolute transport from current meters, BC_{2240} (dashed line) is baroclinic transport defined as \mathcal{T} minus velocity at 2240 dbar times the water depth, and BC_{3320} (fine solid line) is \mathcal{T} minus velocity at 3320 dbar times the water depth



Click on thumbnail for full-sized image.

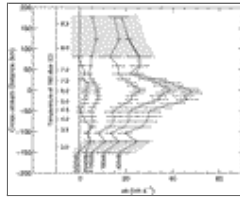
FIG. 15. (a) The term $f^{-1} \partial u / \partial y$ at 420 dbar from smoothed absolute velocity profile. (b) Smoothed absolute velocity profile at current meter levels (thin lines) and locations where condition for barotropic instability is satisfied (thick lines). Mean profiles of vertical velocity shear (c) and squared buoyancy frequency (d) from CTDs in the SAF. (e) Cross-stream gradient of potential vorticity in the SAF



Click on thumbnail for full-sized image.

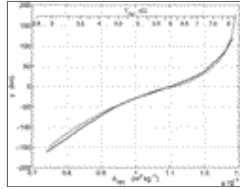
FIG. A1. Scatter of cross-stream gradient of specific volume anomaly vs specific volume anomaly at 780 dbar, with linear least

squares fit either side of $\delta_{780} = 1.102 \times 10^{-6} \text{ m}^3 \text{ kg}^{-1}$, corresponding to $T_{780} = 6^\circ\text{C}$.



[Click on thumbnail for full-sized image.](#)

FIG. A2. Cross-stream profile of along-stream absolute velocity from the method of [Hall and Bryden \(1985\)](#). Standard error is calculated for 10 (5) degrees of freedom in unshaded (shaded) bins



[Click on thumbnail for full-sized image.](#)

FIG. A3. Cross-stream distance calculated using the method of [Hall and Bryden \(1985\)](#) (thin line) compared with cross-stream distance calculated in this paper (thick line)

Corresponding author address: Dr Helen E. Phillips, Woods Hole Oceanographic Institution, MS21, 360 Woods Hole Road, Woods Hole, MA 02543. E-mail: hphillips@whoi.edu

* Current affiliation: Woods Hole Oceanographic Institution, Woods Hole, Massachusetts

[top ▲](#)



© 2008 American Meteorological Society [Privacy Policy and Disclaimer](#)
Headquarters: 45 Beacon Street Boston, MA 02108-3693
DC Office: 1120 G Street, NW, Suite 800 Washington DC, 20005-3826
amsinfo@ametsoc.org Phone: 617-227-2425 Fax: 617-742-8718
[Allen Press, Inc.](#) assists in the online publication of *AMS* journals.